OPEN

Broadband evolution of phononic-crystal-waveguide eigenstates in real- and k-spaces

P. H. Otsuka[1], K. Nanri[1], O. Matsuda[1], M. Tomoda[1], D. M. Profunser[1], I. A. Veres[2], S. Danworaphong[3], A. Khelif[4], S. Benchabane[4], V. Laude[4] & O. B. Wright[1]

[1]Division of Applied Physics, Faculty of Engineering, Hokkaido University, Sapporo 060-8628, Japan, [2]Research Center for Non-Destructive Testing GmbH, Altenberger Str. 69, 4040 Linz, Austria, [3]School of Science, Walailak University, Nakhon Si Thammarat 80160, Thailand, [4]Institut FEMTO-ST, Université de Franche-Comté and CNRS, 32 Avenue de l'Observatoire, F-25044 Besançon, France.

Control of sound in phononic band-gap structures promises novel control and guiding mechanisms. Designs in photonic systems were quickly matched in phononics, and rows of defects in phononic crystals were shown to guide sound waves effectively. The vast majority of work in such phononic guiding has been in the frequency domain, because of the importance of the phononic dispersion relation in governing acoustic confinement in waveguides. However, frequency-domain studies miss vital information concerning the phase of the acoustic field and eigenstate coupling. Using a wide range of wavevectors k, we implement an ultrafast technique to probe the wave field evolution in straight and L-shaped phononic crystal surface-phonon waveguides in real- and k-space in two spatial dimensions, thus revealing the eigenstate-energy redistribution processes and the coupling between different frequency-degenerate eigenstates. Such use of k-t space is a first in acoustics, and should have other interesting applications such as acoustic-metamaterial characterization.

Wavepackets can be tightly controlled by periodic media, such as electrons in solids, light in photonic crystals[1], sound in phononic crystals[2], and coastal water waves in periodic sandbars[3]. Interferences between waves reflected at each unit cell result in complex frequency-wavevector (f-k) relations characterized by frequency ranges of dispersive propagation separated by band gaps in which undamped eigenstates cannot exist. Band-gap physics and technology is the origin of revolutionary advances such as solid-state electronics and, more recently, the science of metamaterials, the latter spawning new fields such as negative refraction, super-resolution focusing, slow light and cloaking[4–6]. Momentum-space-, i.e. k-space-, monitoring of eigenstates directly reveals the physical processes at work in such systems: just as k-space can be used to follow the evolution of quantum eigenstates in atomic[7], solid-state[8], and matter-wave systems[9], it can also be used to follow the progression of quasi-monochromatic wavepackets in photonic crystal waveguides[10]. However, such k-space temporal imaging has not been applied to phononic eigenstates. In this paper we harness ultrafast imaging to achieve this in phononic crystal waveguides, which have never been mapped in the time domain, thus revealing their broadband propagation characteristics in real- and k-spaces, as well as in the frequency domain. Applications of our approach include acoustic-metamaterial characterization.

We investigate structures based on defects in periodic elastic band-gap materials in the form of two-dimensional (2D) surface phononic crystals (PCs)[11–13] formed using microscopic holes in crystalline silicon. Our waveguides support surface-phonon wavepackets near ~1 GHz, and are representative structures in the burgeoning field of phononic crystals[13–22].

Results

Circular holes with spacing $a = 6.2$ μm are milled as square lattices on (100) silicon substrates by dry reactive ion etching, leaving single rows of holes unopened to produce straight or L-shaped waveguides (Fig. 1a and b). The hole top diameter is 5.6 μm and the depth is ~100 μm. The 50 nm polycrystalline chromium coating does not significantly affect surface phonon propagation. The walls of the holes taper outwards and intersect with neighbouring holes at a depth of 3 μm (see Fig. 1d), helping to localize the acoustic energy near the surface. This implies that the surface waves inside the PC regions of the sample (as opposed to inside the waveguide regions) are more
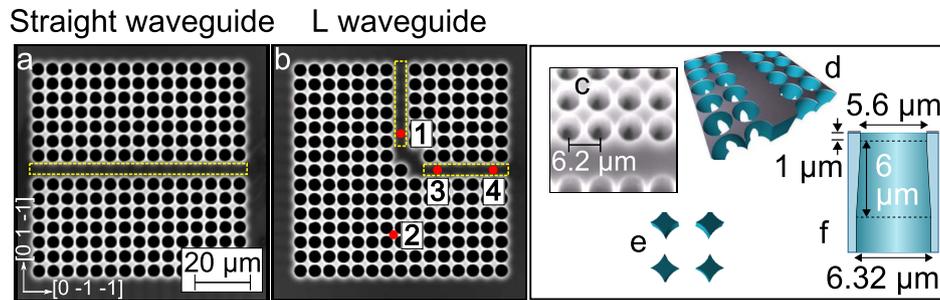
Figure 1 | Phononic crystal samples. (a) and (b) SEM images of the straight and L-shaped PC waveguides. Marked regions are for Fourier analysis. (c) Oblique SEM image (30° to vertical). (d) Simulated structure, (e) its horizontal cross section at a depth >7 μm, and (f) its vertical cross section.

accurately described by Lamb waves rather than Rayleigh waves. The taper is determined from oblique scanning electron microscope (SEM) images (see Fig. 1c).

The 2D acoustic wave field is obtained by the use of an optical pump-and-probe technique combined with a common-path interferometer[23,24]. We capture a series of images with increasing pump-probe delays to build animations (see the Supplementary Information) of the out-of-plane (z-directed) surface velocity over the 12.4-ns laser repetition period at 0.41-ns intervals. Figures 2a–c show a selection of frames (every 10th) from the straight waveguide. The optical pump beam is focused at a point $\ell = 14$ μm outside the left-hand entrance of the waveguide (taking the left-hand edge of the first column of holes as a reference point). The first frame, Fig. 2a, shows the moment ($t = 0$) the pump pulse arrives at the surface. The following frames, Fig. 2b and c at 4.1 and 8.2 ns, respectively, show moments close to when the phonon pulses enter and leave the waveguide. Figures 2d–f show a similar series for the L waveguide ($\ell = 3$ μm).

Time-resolved images superficially reveal the phonon dynamics, but the interaction between the eigenstates remains obscure. When the full complex wave field (i.e. separate amplitude and phase) is available, the temporal evolution in **k**-space can be directly obtained, as in the photonic case[10]. However, for our real sound field $f(\mathbf{r}, t)$ a standard spatial Fourier transform is insufficient to resolve the signs of the wavevectors. This problem can be circumvented by calculating the **k**-t-space amplitude $F_\mathbf{k}(\mathbf{k}, t)$ using the so-called analytic signal[25]:

$$F_\mathbf{k}(\mathbf{k},t) = 2\int_0^\infty F(\mathbf{k},\omega)e^{-i\omega t}d\omega. \qquad (1)$$

$F(\mathbf{k}, \omega)$ is the spatiotemporal Fourier transform of $f(\mathbf{r}, t)$ and ω the angular frequency. A direct spatial Fourier transform only yields $\frac{1}{2}\left(F_\mathbf{k}(\mathbf{k},t) + F_\mathbf{k}^*(-\mathbf{k},t)\right)$, hence we apply Eq. (1) (see also the Supplementary Information). At a single angular frequency ω for wave propagation in two dimensions, there are usually an infinite number of degenerate states which satisfy the dispersion relations $\omega = \omega(\mathbf{k})$. So the Fourier amplitude $F_\mathbf{k}(\mathbf{k}, t)$ contains more information than an analogous function such as $F(\mathbf{r}, \omega, t)$ (that could be obtained through wavelet analysis) and the dispersion relations. Even in the 1D case, one can discuss the scattering between a state **k** and a state −**k** from a knowledge of $F_\mathbf{k}(\mathbf{k}, t)$. Here we show how in our 2D PC waveguides the function $F_\mathbf{k}(\mathbf{k}, t)$ reveals the scattering dynamics.

The insets to the images in Fig. 2a–c show $|F_\mathbf{k}(\mathbf{k}, t)|$ obtained from Eq. (1) for the straight waveguide by integrating to find $F(\mathbf{k}, \omega)$ over the PC region, a 92 μm × 92 μm square, as well as over the region corresponding to the waveguide alone, a 92 μm × 7 μm rectangle in the waveguide (see Fig. 1a). The horizontal curves show the profiles for $k_y = 0$, dominated by waveguide contributions. Interestingly, interference fringes (dependent on the phase), analogous and related to those seen in real space, are evident in the integrations over the PC

regions. In the following we shall see that **k**-t space gives unprecedented information on the phonon dynamics that is impossible to gauge from real space. In Fig. 2a, at 0 ns, the newly-generated phonon pulse is yet to enter the waveguide, but there is a small residual peak at $k_x a/\pi = 0.8$ –this being the main transmission wave number– arising from the previous phonon pulse. In Fig. 2b, at 4.1 ns, a
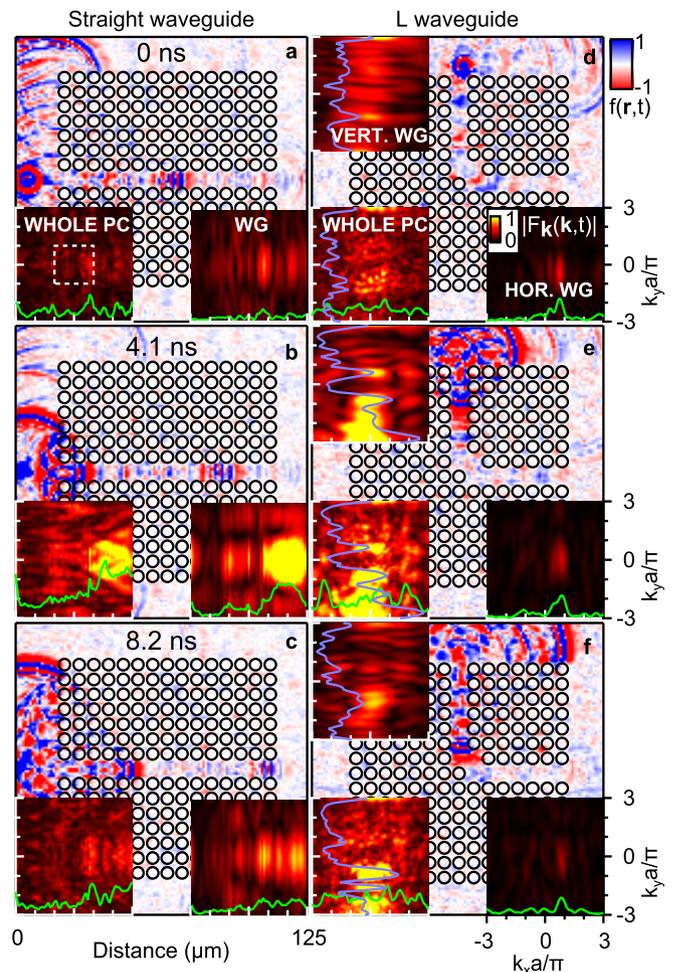

Figure 2 | Wavepacket evolution in real space and k-space. (a)–(c) and (d)–(f): real-time acoustic-field images for the straight and L waveguides (WG), respectively, at 4.1 ns intervals. Insets: 2D **k**-t-space representation for the whole PC region and for the waveguide region(s). The scales for the different times are identical for each type of plot. The scales for the vertical and horizontal sections of the L waveguide are also identical. The horizontal curves are $k_y = 0$ sections through the centre of the guide and, for the L waveguide, the vertical curves are equivalent $k_x = 0$ sections. The white square in (a) shows the 1st Brillouin zone.

2

phonon pulse is just entering the waveguide, producing a large broad peak centred at $k_x a/\pi \approx +2$. The $k_y = 0$ profile at this point roughly corresponds to the broadband spectrum of phonon wavevectors initially excited ($k_x a/\pi \approx 0.2$–3 or wavelength $\lambda = 2\pi/k_x \approx 4$–60 μm). (The broadband acoustic frequency spectrum measured in a region not influenced by the PC waveguide is given in the Supplementary information.) As the wave front moves through the PC and waveguide, the height of this initial peak decreases (Fig. 2c), and transmission peaks emerge and decay, particularly in the waveguide at $k_x a/\pi \approx 0.8$, 1.6 and 2.2. A relatively strong peak, ∼45% of that at $k_x a/\pi = +1$, is also evident in Fig. 2b for the guide near $k_x a/\pi = -1$, a wave number very close to the Bragg scattering condition from the phononic lattice: the shift from $+k_x$ to $-k_x$ is a reciprocal lattice vector **G**, indicating that this peak is a Bloch harmonic[10,24,26] introduced by the periodic waveguide boundaries[14]. The *temporal* dynamics of these peaks is closely related to the *spatial* decay of the corresponding waveguide eigenstates, as shown below quantitatively.

The equivalent series for $|F_k(\mathbf{k}, t)|$ for the L waveguide is shown in Fig. 2d–f. Regions corresponding to the two sections of the waveguide are treated separately (see Fig. 1b and Supplementary Information). The curves are the profiles for $k_x = 0$ (vertical curves–with y axis on the left) and $k_y = 0$ (horizontal curves). The peak near $k_y a/\pi = +0.8$ at 4.1 ns (see Fig. 2d–f and the animation–see Supplementary Information) shows that a significant acoustic amplitude, ∼20%, is reflected at the bend. So in the horizontal section of the waveguide the eigenstate with $k_x a/\pi = +0.8$ has a reduced amplitude, ∼40% of that of the equivalent eigenstate in the vertical section; the transmission around the bend is similar to that calculated for surface phonon waveguides of related design[11], and losses can be explained by scattering to the bulk.

The **k**-*t*-space data is related to two other representations, constant-frequency (**r**-ω) and frequency vs wavevector (ω vs **k**), which complement and validate **k**-*t* space. Frequency-filtered images of $A = |F_\omega(\mathbf{r}, \omega)|$ and $\mathrm{Re}[F_\omega(\mathbf{r}, \omega)] = A\cos\phi$ (ϕ the phase) can be derived from temporal Fourier transforms[24]. Figure 3a and b compare such experimental images of A and $A\cos\phi$ at 322 and 482 MHz. The curves represent the profiles along the centre lines of the waveguides. At 322 MHz both waveguides transmit efficiently; a plausible explanation is the presence of a band gap in the PC, i.e. a stop- or a deaf band[27], where the mode represented by the ω, **k** combination in the waveguide is evanescent in the PC or forbidden by the excitation symmetry, respectively. In contrast, at 482 MHz (and at other frequencies–see Supplementary Information) where we presume a pass band exists in the PC, there is strong attenuation inside both waveguides. (Waves diffracted round and re-entering the waveguides from the right are estimated to have a small influence[28].)

Columns 2 and 4 of Fig. 3 show corresponding results from 3D finite element time domain numerical simulations using the geometry of Fig. 1a–f and impulse forces as periodic sources (see Supplementary Information). The agreement with experiment is good. Sub-surface cross sections (column 4) confirm that at distances 2λ–3λ from the source, the waveguide eigenstates are concentrated within ∼λ from the surface, as expected for Rayleigh-like surface waves. At shorter distances scattering to bulk waves is evident.

To quantify the waveguiding efficiency, we fit a spatially-decaying exponential function to the acoustic amplitude inside the straight waveguide. Figure 4a shows the frequency dependence of the derived decay constant γ (in $e^{-\gamma x}$). At 322, 643 and 964 MHz, γ shows dips, possibly corresponding to frequencies inside PC band gaps[14,15,27]. Similarly, frequencies with large γ should correspond to pass bands. Further evidence for efficient waveguiding can be obtained by considering the wave amplitude A at four different points on the L-waveguide structure[27] shown in Fig. 1b. Figure 4b shows that at points 1, 3 and 4 in the waveguide there are clear peaks at 322 MHz, as expected. Point 1 also has a distinct peak at 643 MHz (the second guiding region of the waveguide). The curve for point 2
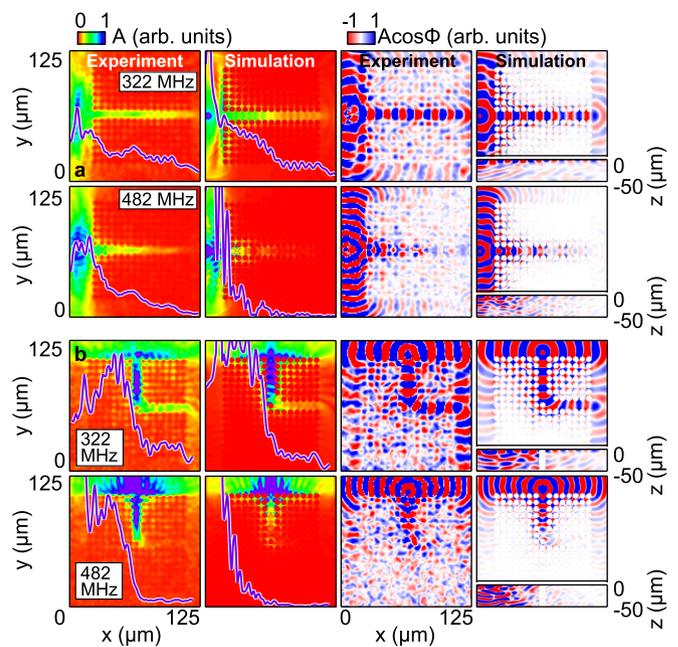

Figure 3 | Frequency-filtered images. r-ω space results. (a) Straight waveguide at 322 MHz (row 1) and 482 MHz (row 2). Columns 1 and 2: maps of the experimental and simulated $A = |F_\omega(\mathbf{r}, \omega)|$, together with sections (vertical curves) through the centre of the waveguide. Columns 3 and 4: $A\cos\phi$. Column 4 includes cross sections in a vertical plane running through the waveguide centres. Both the simulation and experimental data are normalized, with identical scales at the two frequencies in each case. (b) The same for the L waveguide. Cross sections are based on lines or planes though the centre of the waveguide.

shows that acoustic energy does not transmit easily into the PC structure, the highest amplitudes appearing at ∼100 MHz.

We now turn to the ω vs **k** representation, accessible by a dual space-time Fourier transform $F(\mathbf{k}, \omega)$. We extract $|F(\mathbf{k}, \omega)|$ for the same waveguide regions, as shown in Fig. 4d–f for both experiment and simulation, which largely agree. For the straight waveguide (Fig. 4d) the $+k_x$-directed eigenstates are dominant. The slope is nearly linear, as previously predicted in simulations of surface waves in PC waveguides[11,12], and corresponds to a phase velocity, $v_p \approx 5$ km/s, governed by Rayleigh-like waves on the Si substrate[29]. The previously-noted Bloch harmonic, shifted by -2.0 in $k_x a/\pi$, is also visible at 402 MHz. Figure 4g shows the amplitude profiles along the $\pm k_x$ branches of the corresponding dispersion relations, allowing the quantitative comparison of counter-propagating eigenstates. Waveguiding peaks occur at $k_x a/\pi \approx 0.8$, 1.6 and 2.2 (322, 643 and 964 MHz), confirming our previous identifications. The higher frequencies have a greater amplitude, characteristic of the source. As explained later, the reflection coefficients corresponding to these transmission peaks are all very small, ∼10%.

For the L waveguide (Fig. 4e, f and h, i), we divide into vertical (before the bend) and horizontal (after the bend) sections. Only one frequency, 322 MHz, is significantly maintained after the bend, as previously noted in our **k**-*t*-space analysis and evident in the profiles in Fig. 3. The amplitude transmission and reflection coefficients at the bend agree with those measured in **k**-*t* space.

One can now see how **k**-*t* space is related to the spatial decay of eigenstates. Figure 4c shows the measured evolution of the **k**-space amplitude in the straight waveguide at three frequencies, making use of the linear waveguide dispersion relation to convert **k** to ω; at 322 MHz, in the first guiding window, the temporal decay constant is smaller than at the non-guiding frequencies 563 and 804 MHz. Converting the temporal decay constants to spatial ones using the derived v_p gives the crosses in Fig. 4a, in good agreement with γ from
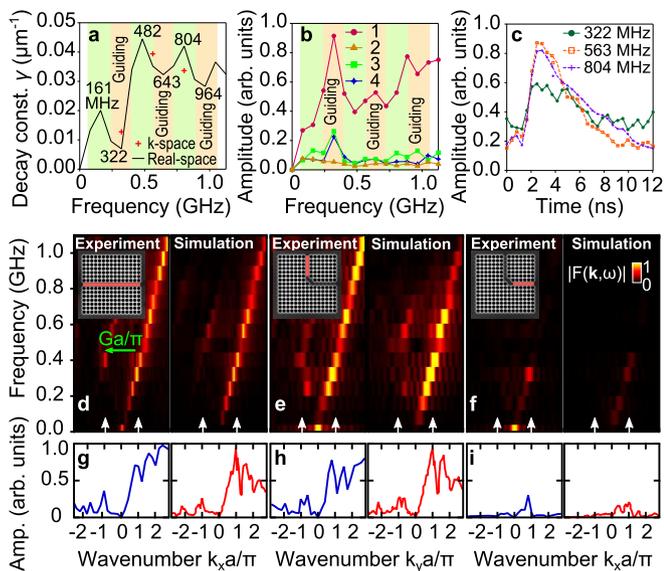
Figure 4 | Dispersion, decay constant, transmission and temporal evolution of eigenstate amplitude. (a) Experimental frequency dependence of γ inside the straight waveguide. The red crosses are fitted values from (c). (b) Point-by-point analysis of the acoustic frequency spectrum in the L waveguide for amplitude $A = |F_\omega(\mathbf{r}, \omega)|$. (c) $\mathbf{k}$-space temporal evolution of the eigenstate amplitude in the straight waveguide. (d)–(f) Experimental and simulated dispersion relations from $|F(\mathbf{k}, \omega)|$ for (d) straight waveguide, and (e), (f) L waveguide (plotted on the same scale). The insets show the analysis regions. Upward pointing white arrows: 1st Brillouin zone. (g)–(i) Profiles of $|F(\mathbf{k}, \omega)|$ taken along the dispersion relation.

$\mathbf{r}$-ω space. (Unlike the latter results, these points are derived without the approximation of ignoring counter-propagating waves–an advantage of using $\mathbf{k}$-t space.) The full temporal evolution of the eigenstate-energy (E) distribution $|F(E, t)|$, sampled by the plots in Fig. 4c, can be viewed as animations in the Supplementary Material together with equivalent simulations.

Discussion

Acoustic energy transmits in and out of the waveguides very easily, as previously noted in numerical calculations[12]. To better understand the origin of this effect we simulated a straight "slab" waveguide of fixed width w equal to that of the straight PC waveguide. Animations in $\mathbf{k}$-t space show a single peak at positive k_x with negligible reflection (see Supplementary Information). In addition, the slab dispersion is found to be linear–evidently a consequence of $\lambda \gtrsim w$–and the attenuation practically zero and frequency-independent. This reveals the physics behind the PC surface-phonon waveguiding: the strong frequency dependences we observe in transmission arise from the periodic nature of the containing medium, and the weak end-reflections and concomitant ease of in-coupling, as well as the low surface-phonon dispersion regions–very different from the highly-dispersive behaviour of bulk waves in PC waveguides exhibiting lateral resonances[13,15]–are inherent in solid PC waveguide structures. In contrast to the strong impedance mismatch at the end of an organ pipe, in which $\sim$100% of the acoustic energy is reflected[30], in such solid waveguides the surface-wave end reflection is strikingly small owing to a relatively low effective impedance mismatch.

In conclusion, by use of the raw wave field we have followed the evolution of a phononic system in both 2D real- and $\mathbf{k}$-spaces for the first time. The acoustic propagation, damping, reflection, and the in- and out-coupling for phononic crystal waveguides are elucidated, and the data corroborated in $\mathbf{r}$-ω and ω vs $\mathbf{k}$ spaces. To our knowledge, animating $\mathbf{k}$-space is new to acoustics, and opens up fascinating possibilities. In addition to the characterization of surface

acoustic wave devices in telecommunications, one could, for example, monitor acoustic pulses passing through new classes of acoustic metamaterials such as acoustic cloaks[31] or negative-index prisms[20]. Our broadband approach to $\mathbf{k}$-t space should also be widely applicable in other fields: extension to ultrafast photonic imaging with attosecond pulses is one possible avenue[32]; modifying angle-resolved photoelectron spectroscopy[8,33] for time-domain probing of electronic states in 2D $\mathbf{k}$-space is another.

Methods

Surface phonons are thermoelastically excited by frequency-doubled optical pulses from a mode-locked Ti:sapphire laser at a wavelength of 415 nm, repetition rate 80.4 MHz, duration $\sim$200 fs, energy per pulse of $\sim$0.15 nJ and a spot diameter at full-width-half-maximum (FWHM) of 1.9 μm on the sample. Out-of-plane motion is detected interferometrically[34] by a pair of 830 nm optical pulses that are separated by a time interval of $\tau \approx 300$ ps and are focused at normal incidence on the surface to a 1.5-μm FWHM diameter spot. We monitor the optical phase difference between two consecutive probe pulses, proportional to the outward surface velocity of a surface particle. (τ is short compared with the minimum phonon period $\sim$1 ns.) Chopping the pump beam at 1 MHz and using a lock-in amplifier allows displacements $\sim$10 pm to be resolved with a precision of $\sim$0.1 pm at 100 Hz bandwidth. Each phonon image is built up by scanning the probe beam relative to the sample while keeping the pump focused on a fixed point at a fixed pump-probe delay time. The continuous repetition of the pump laser source pulses induces a nondestructive local steady-state heating of $\sim$4 K and a transient rise of $\sim$250 K.

1. Joannopoulos, J. D., Villeneuve, P. R. & Fan, S. Photonic crystals: putting a new twist on light. *Nature* **386**, 143–149 (1997).
2. Vasseur, J. O. *et al.* Experimental and theoretical evidence for the existence of absolute acoustic band gaps in two-dimensional solid phononic crystals. *Phys. Rev. Lett.* **86**, 3012–3015 (2001).
3. Mei, C. C. Resonant reflection of surface water waves by periodic sandbars. *J. Fluid Mech.* **152**, 315–335 (1985).
4. Veselago, V. G. & Narimanov, E. E. The left hand of brightness: past, present and future of negative index materials. *Nature Mater.* **5**, 759–762 (2006).
5. Zhang, X. & Liu, Z. Superlenses to overcome the diffraction limit. *Nature Mater.* **7**, 435–441 (2008).
6. Ergin, T., Stenger, N., Brenner, P., Pendry, J. B. & Wegener, M. Three-dimensional invisibility cloak at optical wavelengths. *Science* **328**, 337–339 (2010).
7. Gopal, R. *et al.* Three-dimensional momentum imaging of electron wave packet interference in few-cycle laser pulses. *Phys. Rev. Lett.* **103**, 053001 (2009).
8. Rohwer, T. *et al.* Collapse of long-range charge order tracked by time-resolved photoemission at high momenta. *Nature* **471**, 490–493 (2011).
9. Mark, M. J. *et al.* Demonstration of the temporal matter-wave talbot effect for trapped matter waves. *New J. Phys.* **13**, 085008 (2011).
10. Engelen, R. J. P. *et al.* Ultrafast evolution of photonic eigenstates in k-space. *Nature Phys.* **3**, 401–405 (2007).
11. Sun, J.-H. & Wu, T.-T. Propagation of surface acoustic waves through sharply bent two-dimensional phononic crystal waveguides using a finite-difference time-domain method. *Phys. Rev. B* **74**, 174305 (2006).
12. Tanaka, Y., Yano, T. & Tamura, S. Surface guided waves in two-dimensional phononic crystals. *Wave Motion* **44**, 501–512 (2007).
13. Pennec, Y., Vasseur, J. O., Djafari-Rouhani, B., Dobrzyński, L. & Deymier, P. A. Two-dimensional phononic crystals: Examples and applications. *Surf. Sci. Rep.* **65**, 229–291 (2010).
14. Kafesaki, M., Sigalas, M. M. & Garcia, N. Frequency modulation in the transmittivity of wave guides in elastic-wave band-gap materials. *Phys. Rev. Lett.* **85**, 4044–4047 (2000).
15. Khelif, A., Djafari-Rouhani, B., Vasseur, J. O. & Deymier, P. A. Transmission and dispersion relations of perfect and defect-containing waveguide structures in phononic band gap materials. *Phys. Rev. B* **68**, 024302 (2003).
16. Yang, S. *et al.* Focusing of sound in a 3d phononic crystal. *Phys. Rev. Lett.* **93**, 24301 (2004).
17. Gorishnyy, T., Ullal, C., Maldovan, M., Fytas, G. & Thomas, E. Hypersonic phononic crystals. *Phys. Rev. Lett.* **94**, 115501 (2005).
18. Cheng, W., Wang, J., Ulrich, J., Fytas, G. & Stefanou, N. Observation and tuning of hypersonic bandgaps in colloidal crystals. *Nat. Mater.* **5**, 830 (2006).
19. Ke, M. *et al.* Surface resonant-states-enhanced acoustic wave tunneling in two-dimensional phononic crystals. *Phys. Rev. Lett.* **99**, 44301 (2007).
20. Lu, M. *et al.* Negative birefraction of acoustic waves in a sonic crystal. *Nat. Mater.* **6**, 744–748 (2007).
21. Still, T. *et al.* Simultaneous occurrence of structure-directed and particle-resonance-induced phononic gaps in colloidal films. *Phys. Rev. Lett.* **100**, 194301 (2008).
22. Boechler, N., Theocharis, G. & Daraio, C. Bifurcation-based acoustic switching and rectification. *Nat. Mater.* **10**, 665–668 (2011).
23. Sugawara, Y. *et al.* Watching ripples on crystals. *Phys. Rev. Lett.* **88**, 185504 (2002).

24. Profunser, D. M., Muramoto, E., Matsuda, O., Wright, O. B. & Lang, U. Dynamic visualization of surface acoustic waves on a two-dimensional phononic crystal. *Phys. Rev. B* **80**, 014301–7 (2009).
25. Smith, J. *Mathematics of the Discrete Fourier Transform (DFT) with Audio Applications* (W3K Publishing, http://books.w3k.org/, 2007).
26. Profunser, D. M., Wright, O. B. & Matsuda, O. Imaging ripples on phononic crystals reveals acoustic band structure and bloch harmonics. *Phys. Rev. Lett.* **97**, 055502 (2006).
27. Wu, T.-C., Wu, T.-T. & Hsu, J.-C. Waveguiding and frequency selection of lamb waves in a plate with a periodic stubbed surface. *Phys. Rev. B* **79**, 104306 (2009).
28. At 322 MHz these waves contribute $\lesssim 20\%$ to the $-k_x$ amplitude in the L waveguide.
29. Vines, R. E., Hauser, M. R. & Wolfe, J. P. Imaging of surface acoustic waves. *Z. Phys. B* **98**, 255–271 (1995).
30. Blackstock, D. T. *Fundamentals of Physical Acoustics* (Wiley, New York, 2000).
31. Stenger, N., Wilhelm, M. & Wegener, M. Experiments on elastic cloaking in thin plates. *Phys. Rev. Lett.* **108**, 14301 (2012).
32. Cavalieri, A. L. *et al.* Attosecond spectroscopy in condensed matter. *Nature* **449**, 1029–1032 (2007).
33. Krömker, B. *et al.* Development of a momentum microscope for time resolved band structure imaging. *Rev. Sci. Instrum.* **79**, 053702–053702 (2008).
34. Tachizaki, T. *et al.* Scanning ultrafast sagnac interferometry for imaging two-dimensional surface wave propagation. *Rev. Sci. Instrum.* **77**, 043713 (2006).

Acknowledgments

Author contributions

Additional information